

A fourth-order kernel for improving numerical accuracy and stability in Eulerian and total Lagrangian SPH

Zhentong Wang, Bo Zhang, Oskar J. Haidn, Xiangyu Hu*

TUM School of Engineering and Design, Technical University of Munich, Garching, 85747, Germany

Abstract

The error of smoothed particle hydrodynamics (SPH) using kernel for particle-based approximation mainly comes from smoothing and integration errors. The choice of kernels has a significant impact on the numerical accuracy, stability and computational efficiency. At present, the most popular kernels such as B-spline, truncated Gaussian (for compact support), Wendland kernels have 2nd-order smoothing error and Wendland kernel becomes mainstream in SPH community as its stability and accuracy. Due to the fact that the particle distribution after relaxation can achieve fast convergence of integration error respected to support radius, it is logical to choose kernels with higher-order smoothing error to improve the numerical accuracy. In this paper, the error of 4th-order Laguerre-Wendland kernel proposed by Litvinov et al. [1] is revisited and another 4th-order truncated Laguerre-Gauss kernel is further analyzed and considered to replace the widely used Wendland kernel. The proposed kernel has following three properties: One is that it avoids the pair-instability problem during the relaxation process, unlike the original truncated Gaussian kernel, and achieves much less relaxation residue than Wendland and Laguerre-Wendland ker-

*Corresponding author.

Email addresses: zhentong.wang@tum.de (Zhentong Wang), bo.zhang@tum.de (Bo Zhang), oskar.haidn@tum.de (Oskar J. Haidn), xiangyu.hu@tum.de (Xiangyu Hu)

nels; One is the truncated compact support size is the same as the non-truncated compact support of Wendland kernel, which leads to both kernels' computational efficiency at the same level; Another is that the truncation error of this kernel is much less than that of Wendland kernel. Furthermore, a comprehensive set of $2D$ and $3D$ benchmark cases on Eulerian SPH for fluid dynamics and total Lagrangian SPH for solid dynamics validate the considerably improved numerical accuracy by using truncated Laguerre-Gauss kernel without introducing extra computational effort.

Keywords: Truncated Laguerre-Gauss kernel, Fourth-order, Numerical accuracy, Stability, Computational efficiency, Eulerian SPH, Total Lagrangian SPH

1. Introduction

Smoothed particle hydrodynamics (SPH) is a meshless method originally proposed by Lucy [2], Gingold and Monaghan [3] and has been widely used in fluid dynamics [3], solid mechanics [4], and other scientific and industrial applications [5, 6, 7, 8]. Since the particle-based approximation in SPH is formulated with a Gaussian-like smoothing kernel function with compact support [9], proper choice of the latter is crucial, as already found and explored in Refs. [10, 11, 12], for the numerical accuracy, stability and computational efficiency. Generally, there are two factors determining the accuracy of SPH method, i.e. smoothing and integration errors [13, 1]. While the leading vanishing moments of the kernel function define the smoothing error, the particle summation on neighbor particles within the cut-off radius defines the integration error. The current mainstream kernel functions used in SPH, such as B-spline, Wendland, truncated Gaussian (for compact support) and others, are monotonic and give 2nd-order smoothing error as only the first moment vanishes. Although truncated Gaussian kernel is a nature choice for SPH, it has not been widely used compare to other non-truncated, such as B-spline and Wendland,

kernels. One reason is that, in order to achieve sufficient small integration error, the truncated region is much larger than that of other non-truncated kernels and results in lower computational efficiency. The other reason is that, similarly to B-spline kernel, it causes pair-instability problem in which particles tend to appear pair clumping [14, 11]. In recent years, Wendland kernel has gained popularity in SPH community due to its moderate compact support for sufficient accuracy and ability to overcome pair-instability problem.

With given smoothing kernel, beside the size of compact support, the integration error strongly relies on particle distribution [13]. Litvinov et al. [1] found that particles relaxed from random initial position and constant background pressure is able to achieve the same accuracy as those located on uniform lattice positions. Since relaxed particle distribution can be obtained for complex geometries, it is more applicable than uniform lattice distribution for practical applications. Another finding in Ref. [1] is that, under relaxed particle distribution, the convergence rate of integration error (8th-order respected to support radius) can be much higher than that of smoothing error. Therefore, two non-monotonic, namely truncated Laguerre–Gauss and Laguerre–Wendland, kernels with 4th-order smoothing error has been considered for improving the overall accuracy of SPH approximations. However, these kernels have not been applied for practical SPH algorithms, due to the fact that, for moderate compact support, the actual integration error of Laguerre–Wendland kernel is much larger than that obtained by the original 2nd-order Wendland kernel. Note that, the truncated Laguerre–Gauss kernel has not been tested in Ref. [1] probably due to the above-mentioned pair-instability problem of the original truncated Gaussian kernel.

In the present work, the large integration error of Laguerre–Wendland kernel in moderate compact support is revisited, and the source of error has been analyzed

according to the kernel profiles. Based on this, the truncated Laguerre–Gauss kernel is chosen to improve the overall accuracy of SPH approximations. Quite counter intuitively, further numerical tests show that not only the chosen kernel with moderate neighboring particles does not experience pair-instability problem like the original 2nd-order counterpart, but also able to achieve much less relaxation residue than that of Wendland kernel. The chosen kernel has been applied to Eulerian and total Lagrangian SPH formulations for fluid and solid dynamics problems, respectively. The numerical tests shown that considerable higher accuracy has been achieved compared with that of original Wendland kernel without introducing extra computational effort.

The structure of this paper is as follows: Section 2 gives the preparations of error analysis and revisites Laguerre-Wendland kernel. Also, the errors of Laguerre-Wendland and truncated Laguerre-Gauss kernels are analyzed, and the formulation as well as properties of the latter are discussed in detail. Section 3 introduces standard Eulerian formulation with its extensions and total Lagrangian SPH formulas. The extensions include the incorporation of dissipation limiters to decrease numerical dissipation, the utilization of particle relaxation and kernel correction matrix to ensure zero-order and first-order consistency, respectively. Moving on to Section 4, a series of numerical examples are employed to demonstrate the performance and computational efficiency of the proposed kernel. All computational codes utilized in this study have been made publicly available through the SPHinXsys repository [15], accessible at both <https://www.sphinxsys.org> and <https://github.com/Xiangyu-Hu/SPHinXsys>.

2. Kernel analysis

2.1. Preparations of error analysis

The SPH approximation of gradient of a function field $f(\mathbf{r})$ at a particle position \mathbf{r}_i can be derived as following steps

$$\nabla f(\mathbf{r}_i) \approx \int_V \nabla f(\mathbf{r}) W(\mathbf{r}_i - \mathbf{r}, h) dV = - \int_V f(\mathbf{r}) \nabla W(\mathbf{r}_i - \mathbf{r}, h) dV \approx - \sum_j f(\mathbf{r}_j) \nabla W_{ij} V_j, \quad (1)$$

where V_j is the volume of the neighboring particle j respect to particle i , $W(\mathbf{r}_i - \mathbf{r}, h)$ is a smooth kernel function with h denoting the smoothing length and the gradient of kernel function $\nabla W_{ij} = \nabla W(\mathbf{r}_i - \mathbf{r}_j, h)$. The first step is the smoothing approximation where the Dirac delta function is replaced by a smooth kernel function and introduces the error called smoothing error E_s . The second step is integration by parts following the assumption that the kernel function is zero at the domain boundary. The third step is the approximated integration by summation over all neighboring particles and introduces the error called integration error E_r . Afterwards, the truncation error E_t is given by $E_t = E_s + E_r$. For simplicity of writing, we simplify $f(\mathbf{r})$ at position \mathbf{r}_i and \mathbf{r}_j to f_i and f_j respectively in the following content. Following Ref. [16], Eq. (1) can be modified in a strong form as

$$\nabla f_i = \nabla f_i - f_i \nabla 1 \approx \sum_j f_{ij} \nabla W_{ij} V_j, \quad (2)$$

with $f_{ij} = f_i - f_j$. Also, the modification in a weak form as

$$\nabla f_i = \nabla f_i + f_i \nabla 1 \approx -2 \sum_j \bar{f}_{ij} \nabla W_{ij} V_j, \quad (3)$$

with $\bar{f}_{ij} = (f_i + f_j)/2$. Due to the fact that the weak form is applied in the momentum conservation equations, we employ Eq. (3) to investigate the error estimation in

the later section. As is mentioned, the particle distribution plays a crucial role in influencing the integration error [1, 17]. Therefore, to achieve a high-quality particle distribution in practical applications and ensure zero-order consistency, i.e. $\sum_j V_j \nabla W_{ij} = \mathbf{0}$, we employ particle relaxation [18] before the error analysis and the acceleration in the process is calculated by

$$\mathbf{a}_i = -\frac{2}{\rho_i} \sum_j V_j \nabla W_{ij}, \quad (4)$$

with m denoting the mass. Note that the SPH approximation for the derivative of kernel function directly influence the flux calculation in conservation equations, we further introduce the kernel correction matrix [5] given by

$$\mathbf{B}_i = -\left(\sum_j \mathbf{r}_{ij} \otimes \nabla W_{ij} V_j \right)^{-1} \quad (5)$$

to compensate the error and satisfy the first-order consistency.

2.2. Error analysis using Laguerre-Wendland kernel

As shown in Litvinov et al. [1], Laguerre-Wendland and Laguerre-Gauss kernels have the second vanishing moment and 4th-order smoothing error. Also, the former had been studied in Litvinov et al. [1] but has not employed in practice due to its larger integration error than the widely used Wendland kernel. Here, we revisit this kernel to explore the reason for the excessive integration error. By comparing the profiles of the kernels and their derivatives, as shown in Figure 1, we find that the gradient magnitude of Laguerre-Wendland kernel is much larger than that of Wendland kernel. Note that the SPH approximation is highly relied on the size of compact support, which is usually adopted as $2h$ in practice where smoothing length $h = \kappa dp$ with dp denoting the initial particle spacing and κ determining the number of neighboring particles. With these observations, it is straightforward to consider that

the possible reason for Laguerre-Wendland kernel introducing larger integration error is that the number of neighboring particles is insufficient to resolve the large gradient magnitude within a moderate compact support. Based on this, we apply different κ including $\kappa = 1.3, 2.0$ and 2.5 meaning different total number of neighboring particles for analysing the integration error. Note that the corresponding resolutions are adopted according to the different κ to keep smoothing length constant, i.e. the smoothing error is unchanged. For the quantitative analysis, following Eq. (3), L_1 and L_{infinity} normalizations are given by

$$\begin{cases} L_1(df/dx) = \frac{1}{N} \sum_i \left| \nabla f_i - 2 \sum_j \bar{f}_{ij} \nabla W_{ij} V_j \right| \\ L_{\text{infinity}}(df/dx) = \max_i \left| \nabla f_i - 2 \sum_j \bar{f}_{ij} \nabla W_{ij} V_j \right| \end{cases}, \quad (6)$$

with N and df/dx denoting the total number of particles and the derivative of the function field, respectively. Here, the error obtained in Eq. (6) is the truncation error. When a sufficient number of neighboring particles is present and the truncation error cannot be further reduced due to the negligible impact of the integration error, the dominant factor in the truncation error is the smoothing error. Conversely, when an insufficient number of neighboring particles is available, the integration error takes the lead in contributing to the overall truncation error.

In the study, a circular geometry of a diameter $D = 2$ with the resolution $dp = 1/60$ is applied and we test the SPH approximation for the derivatives of an constant function $f = 1$ and a trigonometric function $f = \sin(2\pi x)$ using Wendland and Laguerre-Wendland kernels without and with the kernel correction matrix in this domain with the respective particle distributions obtained by their own kernels shown in Figure 2, and Tables 1 and 2 list the truncation errors with different κ . Note that the boundary particles are not considered in the kernel analysis due to the fact that these particles are given the assigned values and do not evaluate the kernel

Table 1: Truncation errors of the SPH approximation for df/dx with $f = 1$ and $f = \sin(2\pi x)$ using Wendland and Laguerre-Wendland kernels with different κ without the kernel correction matrix.

Truncation errors	κ	$L_1(df/dx)$		$L_{\text{infinity}}(df/dx)$	
		$f = 1$	$f = \sin(2\pi x)$	$f = 1$	$f = \sin(2\pi x)$
Wendland	1.3	0.034	0.123	0.259	0.400
Laguerre-Wendland		0.070	0.673	1.880	3.506
Wendland	2.0	0.014	0.073	0.027	0.150
Laguerre-Wendland		0.010	0.018	0.028	0.046
Wendland	2.5	0.018	0.078	0.032	0.161
Laguerre-Wendland		0.005	0.009	0.017	0.030

Table 2: Truncation errors of the SPH approximation for df/dx with $f = 1$ and $f = \sin(2\pi x)$ using Wendland and Laguerre-Wendland kernels with different κ with the kernel correction matrix.

Truncation errors	κ	$L_1(df/dx)$		$L_{\text{infinity}}(df/dx)$	
		$f = 1$	$f = \sin(2\pi x)$	$f = 1$	$f = \sin(2\pi x)$
Wendland	1.3	0.039	0.052	0.209	0.187
Laguerre-Wendland		0.077	0.067	2.334	2.319
Wendland	2.0	0.014	0.042	0.026	0.067
Laguerre-Wendland		0.011	0.007	0.029	0.028
Wendland	2.5	0.018	0.043	0.033	0.068
Laguerre-Wendland		0.005	0.003	0.017	0.015

gradient. From the results, the truncation errors using Laguerre-Wendland kernel exhibit similar behavior to those obtained with Wendland kernel, declining with $\kappa \leq 2$ and remaining relatively unchanged at $\kappa = 2.5$. These results suggest that, while the smoothing error dominates at $\kappa \geq 2$, the integration error takes the lead at $\kappa = 1.3$. For the condition of smoothing error dominant with $\kappa \geq 2$, it is implied that the smoothing error of Laguerre-Wendland kernel is less than Wendland kernel, which agrees with the property of kernels' smoothing order. In addition, given the reasonable truncation errors, while the impact of the kernel correction matrix on reducing the truncation error with the derivative of $f = 1$ is not as apparent, this matrix can further minimize the error with that of $f = \sin(2\pi x)$ effectively, suggesting that the kernel correction matrix has distinct effects on higher-order terms.

2.3. Truncated Laguerre-Gauss kernel

As another 4th-order kernel, as shown in Figure 1, Laguerre-Gauss kernel with smaller gradient magnitude than Laguerre-Wendland kernel can be seen as a potential option for not introducing excessive integration error.

2.3.1. Fundamentals of truncated Laguerre-Gauss kernel

The expression of Laguerre-Gauss kernel [1] is given by

$$w(s) = \pi^{-1} L_1^{(1)}(s^2) e^{-s^2}, \quad (7)$$

where $L_1^{(1)}$ denotes the generalized Laguerre polynomial with non-negative Fourier transform and vanishing second-order moment as well as $s = |\mathbf{r}|/h$. For implementing the kernel in practice, we truncate compact domain to $2h$ and give the expression for truncated Laguerre-Gauss kernel as

$$w(s) = \alpha_d \begin{cases} (1 - \frac{s^2}{2} + \frac{s^4}{6}) e^{-s^2} & \text{if } 0 \leq s \leq 2 \\ 0 & \text{if } s > 2 \end{cases}, \quad (8)$$

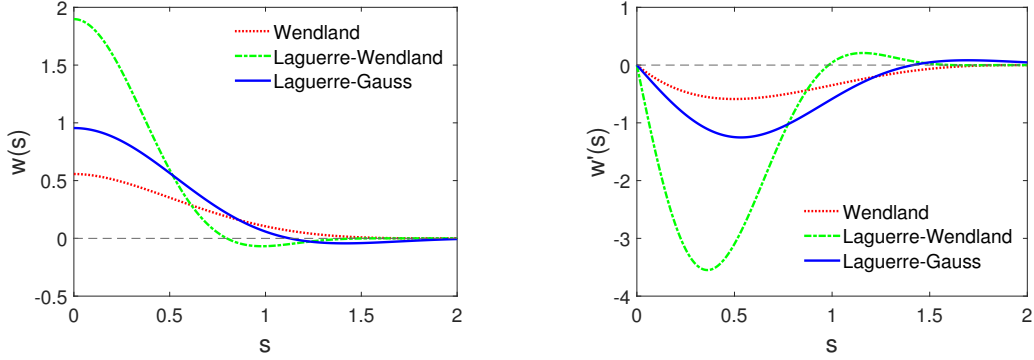


Figure 1: Laguerre-Gauss kernel and the comparison with Wendland as well as Laguerre-Wendland kernels with compact support as $2h$: kernel functions (left panel) and their derivatives (right panel).

where α_d is the normalized coefficient in d dimensional space with the value of $\alpha_1 = 8/(5 \times \sqrt{\pi})$, $\alpha_2 = 3/\pi$ and $\alpha_3 = 8/\pi^{3/2}$. Also, the truncated Laguerre-Gauss kernel and its derivative and the comparisons with Wendland as well as Laguerre-Wendland kernels are presented in Figure 1 showing that its gradient magnitude is larger than that of Wendland kernel but smaller than that of Laguerre-Wendland kernel and the value of kernel function at $2h$ is close to 0. In numerical simulations, to avoid adding extra computational effort, we apply the compact support as $2h$ with smoothing length $h = 1.3dp$, meaning that the computational efficiency using truncated Laguerre-Gauss kernel is the same as that using Wendland kernel.

2.3.2. Performance in stability

To exploit the properties of truncated Laguerre-Gauss kernel, we firstly investigate and compare the relaxed particle distribution using Wendland, Laguerre-Wendland and truncated Laguerre-Gauss kernels in the same circular domain mentioned above. Figure 2 shows the relaxation residue ranging from 3.4×10^{-6} to 4.0×10^{-2} using Wendland, Laguerre-Wendland and truncated Laguerre-Gauss ker-

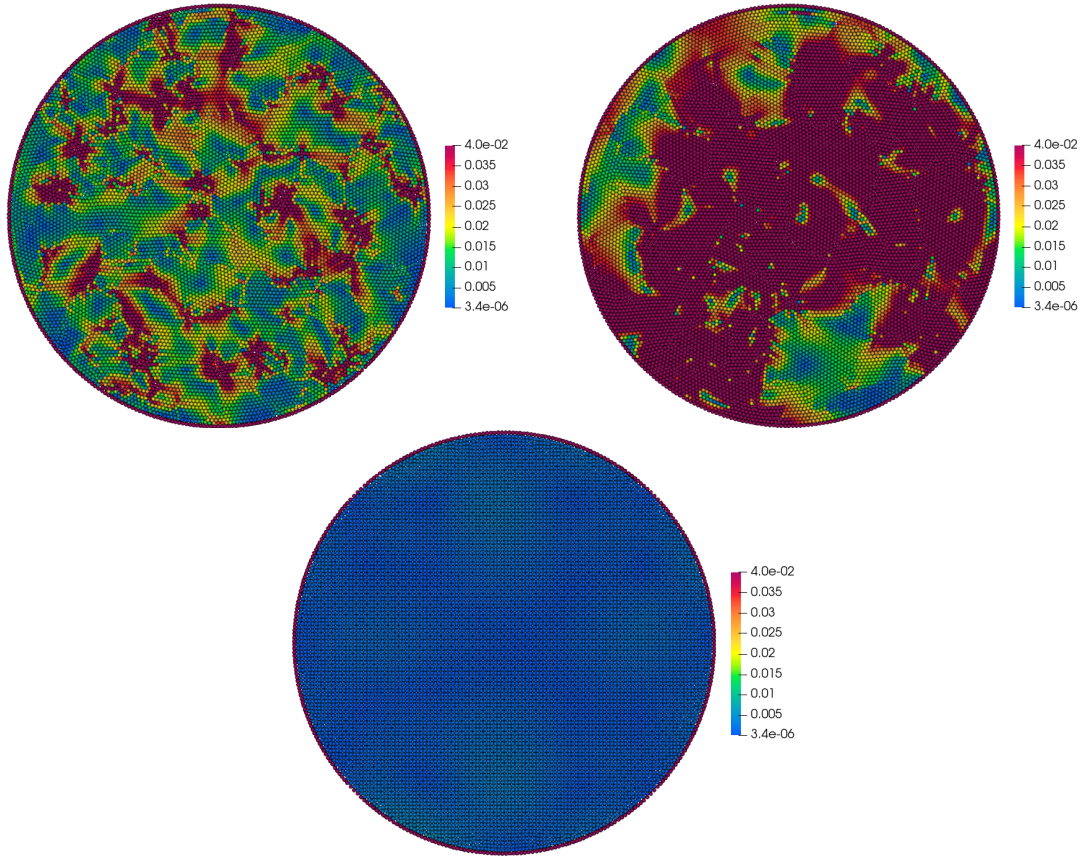


Figure 2: Particle relaxation residue ranging from 3.4×10^{-6} to 4.0×10^{-2} using Wendland (top left panel), Laguerre-Wendland (top right panel) and truncated Laguerre-Gauss (bottom panel) kernels at the final relaxation iteration with the spatial resolution $dp = 1/60$. In the case, the boundary particles are not considered due to its not relying on kernel approximation. Based on this, the average relaxation residue and the variation between the maximum and minimum relaxation residues using truncated Laguerre-Gauss kernel are approximately 0.004 and 0.011, respectively, which are approximately one-tenth and one-twentieth of the values using Wendland kernel. Meanwhile, the average relaxation residue of 0.07 when employing Laguerre-Wendland kernel is approximately twenty times larger than that of using truncated Laguerre-Gauss kernel and the maximum relaxation residue of 1.88 appears to be unreasonable.

nels at the final relaxation iteration. Completely contrary to our intuition that truncated Laguerre-Gauss kernel is similar to original truncated Gaussian kernel in that it suffers from pair-instability problem with $\kappa = 1.3$, it can be observed that the particle relaxation using truncated Laguerre-Gauss kernel does not appear this problem. Similarly with the kernel analysis in section 2.2, the particles in the boundary are also omitted in the following analysis. Based on this, truncated Laguerre-Gauss kernel yields an average relaxation residue of 0.004 and a variation between the maximum and minimum relaxation residues of 0.011 and these values represent roughly one-tenth and one-twentieth of those obtained using Wendland kernel. Besides, Laguerre-Wendland kernel results in an average relaxation residue of 0.07, which is approximately twenty times larger than that observed with truncated Laguerre-Gauss kernel. However, the maximum relaxation residue of 1.880 using Laguerre-Wendland kernel is unacceptable and unreasonable. Therefore, truncated Laguerre-Gauss kernel ensures the numerical stability and obtains higher-quality particle distribution.

2.3.3. Performance in accuracy

Similarly with the analysis of Laguerre-Wendland kernel, we test the SPH approximation for the derivatives of same functions using truncated Laguerre-Gauss kernel to further verify the approximation accuracy. Specifically, the truncation error using the derivative of function $f = 1$ is equal to the relaxation residue in Eq. (4).

Tables 3 and 4 list the truncation errors using truncated Laguerre-Gauss kernel. From the results, the truncation error in the case of insufficient number of neighboring particles with $\kappa = 1.1$ is still relatively large. Besides, the large errors obtained with $\kappa = 1.6$ is due to the pair instability when the number of neighboring particles is

Table 3: Truncation errors of the SPH approximation for df/dx with $f = 1$ and $f = \sin(2\pi x)$ using truncated Laguerre-Gauss kernel with different κ without the kernel correction matrix.

Truncation errors	κ	$L_1(df/dx)$		$L_{\text{infinity}}(df/dx)$	
		$f = 1$	$f = \sin(2\pi x)$	$f = 1$	$f = \sin(2\pi x)$
	1.1	0.021	0.259	0.614	1.253
Laguerre-Gauss	1.3	0.004	0.123	0.011	0.204
	1.6	0.007	0.210	0.822	0.817

Table 4: Truncation errors of the SPH approximation for df/dx with $f = 1$ and $f = \sin(2\pi x)$ using truncated Laguerre-Gauss kernel with different κ with the kernel correction matrix.

Truncation errors	κ	$L_1(df/dx)$		$L_{\text{infinity}}(df/dx)$	
		$f = 1$	$f = \sin(2\pi x)$	$f = 1$	$f = \sin(2\pi x)$
	1.1	0.021	0.061	0.603	0.448
Laguerre-Gauss	1.3	0.004	0.004	0.011	0.009
	1.6	0.006	0.024	0.784	0.364

too large. Note that $\kappa = 1.3$ is applied in practice as mentioned above to avoid extra computational effort. In the case of $\kappa = 1.3$ with the derivative of latter function, we observe that the truncation errors using truncated Laguerre-Gauss kernel in Table 3 and Wendland kernel in Table 1 are comparable without the utilization of the kernel correction matrix. However, the truncation error using the proposed kernel in Table 4 is significantly smaller than the errors using Wendland and Laguerre-Wendland kernels in Table 2, demonstrating that the former kernel cooperation with the kernel correction matrix offers much higher accuracy. This finding suggests the integration error using truncated Laguerre-Gauss kernel is lower compared to the other two kernels as the integration errors are dominant in using Wendland and Laguerre-Wendland kernels with $\kappa = 1.3$. Furthermore, the proposed kernel exhibits superior performance with respect to the average relaxation residue and the variation of the maximum and minimum residue. Specifically, in Tables 3, the average relaxation residue and the variation are 0.004 and 0.011, respectively, which are approximately one-tenth and one-twentieth of the values listed in Tables 1 for the Wendland kernel, proving that truncated Laguerre-Gauss kernel enables obtain much less average relaxation residue and the variation than those using the other two kernels and these results agree with the particle distribution shown in Figure 2.

3. Governing equations and SPH methods

Here, we consider an extended Eulerian SPH method for fluid dynamics [3] and the standard total Lagrangian SPH method for solid mechanics [4, 19].

3.1. Extended Eulerian SPH

3.1.1. Governing equations

The conservation equations in the Eulerian framework can be described by

$$\frac{\partial \mathbf{U}}{\partial t} + \nabla \cdot \mathbf{F}(\mathbf{U}) = 0, \quad (9)$$

where \mathbf{U} is the vector of the conserved variables, $\mathbf{F}(\mathbf{U})$ the corresponding fluxes.

Here, they can be expressed specifically as

$$\mathbf{U} = \begin{bmatrix} \rho \\ \rho u \\ \rho v \\ \rho w \\ E \end{bmatrix}, \quad \mathbf{F} = \begin{bmatrix} \rho u \\ \rho u^2 + p \\ \rho uv \\ \rho uw \\ u(E + p) \end{bmatrix} + \begin{bmatrix} \rho v \\ \rho vu \\ \rho v^2 + p \\ \rho vw \\ v(E + p) \end{bmatrix} + \begin{bmatrix} \rho w \\ \rho wu \\ \rho wv \\ \rho w^2 + p \\ w(E + p) \end{bmatrix}, \quad (10)$$

where u , v and w are the components of velocity, ρ and p denote the density and pressure, respectively. Here, $E = \frac{\rho \mathbf{v}^2}{2} + \rho e$ is the total energy per volume with e the internal energy. The equation of state (EOS) is added to close the Eq. (9) by

$$p = \begin{cases} \rho(\gamma - 1)e & \text{For compressible flows} \\ c^2(\rho - \rho_0) & \text{For weakly-compressible flows} \end{cases}, \quad (11)$$

where γ is the heat capacity ratio, ρ_0 the reference density. Following the ideal gas equation in compressible flows and the weakly-compressible assumption in incompressible flows, the speed of sound is derived by

$$c = \begin{cases} \sqrt{\frac{\gamma p}{\rho}} & \text{For compressible flows} \\ 10U_{max} & \text{For weakly-compressible flows} \end{cases}. \quad (12)$$

Here, U_{max} the maximum velocity in the flow field to control the density variation less than 1%. Note that the energy equation is turned off in weakly-compressible flows. In the viscous weakly-compressible flows, we add a viscous force given by

$$\left(\frac{\partial \mathbf{v}}{\partial t}\right)^{(v)} = \eta \nabla^2 \mathbf{v} \quad (13)$$

to the momentum equation.

3.1.2. Standard Eulerian SPH discretization

Following Ref. [20], the discretization form of the Eq. (9) can be written as

$$\begin{cases} \frac{\partial}{\partial t} (w_i \rho_i) + 2w_i \sum_j w_j (\rho \mathbf{v})_{E,ij}^* \cdot \nabla W_{ij} = 0 \\ \frac{\partial}{\partial t} (w_i \rho_i \mathbf{v}_i) + 2w_i \sum_j w_j [(\rho \mathbf{v} \otimes \mathbf{v})_{E,ij}^* + p_{E,ij}^* \mathbb{I}] \cdot \nabla W_{ij} = 0, \\ \frac{\partial}{\partial t} (w_i E_i) + 2w_i \sum_j w_j [(E \mathbf{v})_{E,ij}^* + (p \mathbf{v})_{E,ij}^*] \cdot \nabla W_{ij} = 0 \end{cases} \quad (14)$$

where w represents the volume of particle, \mathbf{v} the velocity, \mathbb{I} the identity matrix and terms $(\)_{E,ij}^*$ are solution of the Riemann problem [20]. Here, $\nabla W_{ij} = \frac{\partial W_{ij}}{\partial r_{ij}} \mathbf{e}_{ij}$ denotes kernel gradient where $\mathbf{e}_{ij} = -\mathbf{r}_{ij}/r_{ij}$ with \mathbf{r}_{ij} the displacement pointing from particle j to i .

To obtain the solution of the Riemann problem, three waves with the smallest speed S_l , middle speed S_* and largest speed S_r are utilized. Note that the middle wave distinguishes the two intermediate states as (ρ_l^*, u_l^*, p_l^*) and (ρ_r^*, u_r^*, p_r^*) . For compressible flows, we employ the HLLC Riemann solver [21, 22] because of its ability in capturing the shock discontinuity, with the three wave speeds estimated as

$$\begin{cases} S_l = u_l - c_l \\ S_r = u_r + c_r \\ S_* = \frac{\rho_r u_r (S_r - u_r) + \rho_l u_l (u_l - S_l) + p_l - p_r}{\rho_r (S_r - u_r) + \rho_l (u_l - S_l)} \end{cases} \quad (15)$$

Then, the intermediate states can be calculated as

$$\begin{cases} p^* = p_l + \rho_l (u_l - S_l) (u_l - u^*) = p_r + \rho_r (S_r - u_r) (u^* - u_r) \\ \mathbf{v}_{l/r}^* = u^* \mathbf{e}_{ij} + [\frac{1}{2}(\mathbf{v}_l + \mathbf{v}_r) - \frac{1}{2}(u_l + u_r)\mathbf{e}_{ij}] \\ \rho_{l/r}^* = \rho_{l/r} \frac{(S_{l/r} - q_{l/r})}{(S_{l/r} - u^*)} \\ E_{l/r}^* = \frac{(S_{l/r} - q_{l/r})E_{l/r} - p_{l/r}q_{l/r} + p^*u^*}{S_{l/r} - u^*} \end{cases}, \quad (16)$$

where q represents the velocity magnitude and $u^* = S_*$. In weakly-compressible flows, the intermediate states follows the assumption satisfying $p_l^* = p_r^* = p^*$ and $u_l^* = u_r^* = u^*$ and then a linearised Riemann solver can be expressed as [23, 24]

$$\begin{cases} u^* = \frac{u_l + u_r}{2} + \frac{1}{2} \frac{(p_L - p_R)}{\bar{\rho}\bar{c}} \\ p^* = \frac{p_l + p_r}{2} + \frac{1}{2} \bar{\rho}\bar{c} (u_l - u_r) \end{cases}, \quad (17)$$

with $\bar{\rho}$ and \bar{c} interface-particle averages.

3.1.3. Eulerian SPH extensions

In this section, we implement the particle relaxation following Eq. (4) and kernel correction matrix following Eq. (5) and detail the dissipation limiters, which are used to improve stability and accuracy of Eulerian SPH method. To maintain the conservation property, the corrected kernel gradient can be re-evaluated as

$$\nabla' W_{ij} = \frac{\mathbf{B}_i + \mathbf{B}_j}{2} \nabla W_{ij} \quad (18)$$

to replace the original kernel gradient ∇W_{ij} in Eq. (14).

In order to reduce the numerical dissipation introduced by the Riemann problem, dissipation limiters [24, 25] are implemented and can greatly improve numerical accuracy. In the HLLC Riemann solver, the middle wave speed and pressure in Eq. (16) with the limiter can be rewritten as

$$\begin{cases} u^* = \frac{\rho_l u_l c_l + \rho_r u_r c_r}{\rho_l c_l + \rho_r c_r} + \frac{p_l - p_r}{\rho_l c_l + \rho_r c_r} \beta_{HLLC}^2 \\ p^* = \frac{p_l + p_r}{2} + \frac{1}{2} \beta_{HLLC} [\rho_r c_r (u^* - u_r) - \rho_l c_l (u_l - u^*)] \end{cases}, \quad (19)$$

with the limiter as

$$\beta_{HLLC} = \min \left(\eta_{HLLC} \max \left(\frac{u_l - u_r}{\bar{c}}, 0 \right), 1 \right), \quad (20)$$

where $\eta_{HLLC} = 1.0$ according the numerical tests. Also, the linearised Riemann solver in Eq. (17) with the limiter can be rewritten as

$$\begin{cases} u^* = \frac{u_l + u_r}{2} + \frac{1}{2} \beta_{linearisd}^2 \frac{(p_L - p_R)}{\bar{\rho} \bar{c}} \\ p^* = \frac{p_l + p_r}{2} + \frac{1}{2} \beta_{linearisd} \bar{\rho} \bar{c} (u_l - u_r) \end{cases}, \quad (21)$$

with the dissipation limiter $\beta_{linearisd}$ as

$$\beta_{linearisd} = \min \left(\eta_{linearisd} \max \left(\frac{u_l - u_r}{\bar{c}}, 0 \right), 1 \right). \quad (22)$$

where $\eta_{linearisd} = 15.0$.

3.2. Total Lagrangian SPH

In total Lagrangian SPH framework for elastic solid dynamics, the mass and momentum conservation equations can be expressed as

$$\begin{cases} \rho = J^{-1} \rho^0 \\ \rho^0 \frac{d\mathbf{v}_i}{dt} = \nabla^0 \cdot \mathbb{P}^T \end{cases}, \quad (23)$$

with ρ^0 and ρ the initial and current density, respectively. Here, $J = \det(\mathbb{F})$ with \mathbb{F} denoting the deformation gradient tensor, \mathbf{v} represents the velocity, and \mathbb{P} as well as T are the first Piola-Kirchhoff stress tensor and the matrix transposition operator, respectively. Also, \mathbb{P} can be derived as $\mathbb{P} = \mathbb{F}\mathbb{S}$ with \mathbb{S} the second Piola-Kirchhoff stress tensor where the constitutive equation [15] when the material is linear elastic and isotropic is given by

$$\mathbb{S} = \lambda \text{tr}(\mathbb{E})\mathbb{I} + 2G\mathbb{E}, \quad (24)$$

with λ and G denoting the Lamé parameter and the shear modulus, respectively.

Then, the momentum equation in Eq. (23) with the weak form [15] of the SPH particle approximation can be discretized as

$$\rho_i^0 \frac{d\mathbf{v}_i}{dt} = \sum_j \left(\mathbb{P}_i \mathbf{B}_i^{0\text{T}} + \mathbb{P}_j \mathbf{B}_j^{0\text{T}} \right) \cdot \nabla^0 W_{ij} V_j^0, \quad (25)$$

where $\nabla^0 W_{ij} = \frac{\partial W(\mathbf{r}_{ij}^0, h)}{\partial \mathbf{r}_{ij}^0} \mathbf{e}_{ij}^0$ and \mathbf{B}^0 are the kernel gradient and correction matrix in the initial configuration, respectively. In addition, the deformation change rate is updated with the strong form of the SPH particle approximation as follows:

$$\frac{d\mathbb{F}}{dt} = \sum_j V_j^0 (\mathbf{v}_j - \mathbf{v}_i) \cdot \nabla^0 W_{ij} \mathbf{B}_i^0. \quad (26)$$

4. Numerical results

In this section, a set of numerical simulations including fluid dynamics and elastic solid dynamics are tested to verify the accuracy and computational efficiency of truncated Laguerre-Gauss kernel (denoted as Laguerre-Gauss) and comparison with Wendland kernel [26] (denoted as Wendland). For clarity, the cut-off radius of both kernels is $2.6dp$.

4.1. The Shu-Osher problem

In this part, a one-dimensional Shu-Osher problem is studied to investigate the accuracy of Laguerre-Gauss kernel in the compressible flow. The initial condition is given by

$$(\rho, u, v, p) = \begin{cases} (3.857143, 2.629369, 0, 10.3333) & x \leq 1 \\ (1+0.2\sin(5x), 0, 0, 1) & \text{otherwise} \end{cases}, \quad (27)$$

with the domain $x \in [0, 10]$ and final time $t = 1.8$. Also, three spatial resolutions $dp = 1/200$, $dp = 1/400$ and $dp = 1/800$ are applied for the convergence study.

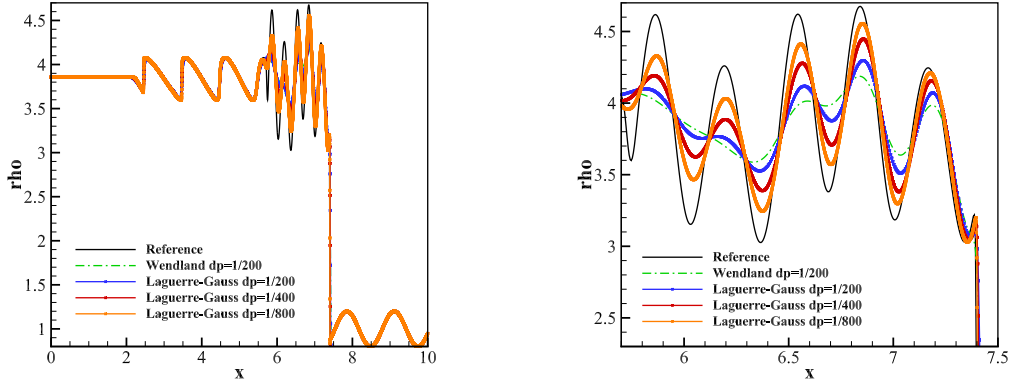


Figure 3: The Shu-Osher problem: Density profile (left panel) and zoom-in view (right panel) using Wendland and Laguerre-Gauss kernels and their comparisons against the reference data [27].

Figure 3 shows the density and zoom-in view profiles using Wendland and Laguerre-Gauss kernels and the comparisons with the reference data [27]. It can be seen that Laguerre-Gauss kernel can significantly improve the accuracy compared to Wendland kernel at the resolution $dp = 1/200$. Also, the results converge rapidly as the resolution increases and there is roughly first-order convergence at the extremities, and second-order convergence in regions other than the extremities.

4.2. Taylor-Green vortex flow

In this section, we consider the two-dimensional viscous Taylor-Green vortex flow to validate the proposed kernel in the weakly-compressible flow. Following Ref. [28], the initial velocity in a unit domain with the periodic boundary conditions in x - and y - directions is given by

$$\begin{cases} u(x, y, t) = -\exp^{bt} \cos(2\pi x) \sin(2\pi y) \\ v(x, y, t) = \exp^{bt} \sin(2\pi x) \cos(2\pi y) \end{cases}, \quad (28)$$

where the decay rate is $b = -8\pi^2/Re$, the Reynolds number $Re = 100$, the total

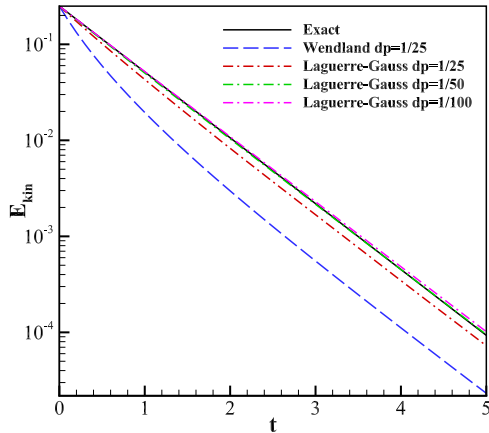


Figure 4: Taylor-Green vortex flow ($Re = 100$): Decay of the kinetic energy using Wendland and Laguerre-Gauss kernels and the comparisons with the theoretical solution (denoted as "Exact").

kinetic energy decay rate $-16\pi^2/Re$ and the final time $t = 5$. Also, we apply three resolutions including $dp = 1/25$, $1/50$ and $1/100$ to test the convergence study.

Figure 4 portrays the kinetic energy decay using Wendland and Laguerre-Gauss kernels and the comparison with the theoretical solution (denoted as "Exact"). From the curves of kinetic energy decay, the method using Laguerre-Gauss kernel shows clearly improved accuracy by reducing the numerical dissipation more effectively at a resolution of $dp=1/25$, and the results achieve second-order convergence as the resolution increases.

4.3. Flow around a cylinder

In this section, flow around a cylinder case containing complex geometries is studied to investigate the versatility of the proposed kernel. In order to assess the numerical results quantitatively, the drag and lift coefficients are given as

$$C_D = \frac{2F_D}{\rho_\infty u_\infty^2 A}, C_L = \frac{2F_L}{\rho_\infty u_\infty^2 A}, \quad (29)$$

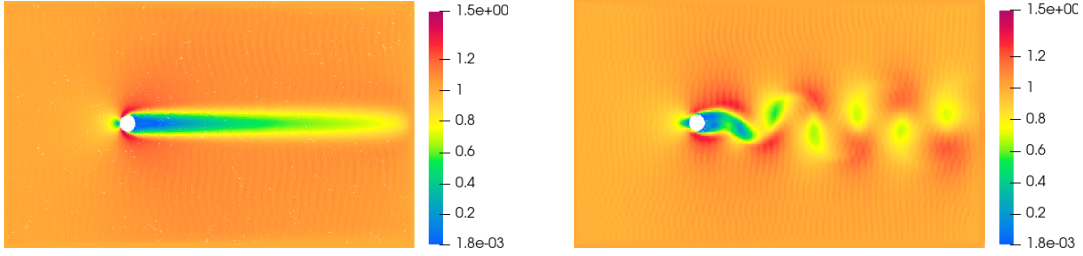


Figure 5: Flow around a cylinder: Velocity contour ranging from 1.8×10^{-3} to 1.5 using Wendland (left panel) and Laguerre-Gauss (right panel) kernels with $Re = 100$ under the resolution $dp = 1/6$ at $t = 300$.

where F_D and F_L denote the drag and lift force on the cylinder respectively and velocity u_∞ as well as density ρ_∞ in the far-field are set as 1. Also, the Strouhal number $St = fD/u_\infty$ in the unsteady cases and the Reynolds numbers $Re = \rho_\infty u_\infty D/\mu$ is 100 with the cylinder diameter $D = 2$ in the case where the far-field boundary conditions are applied in all boundaries and the computational time is $t = 300$. To alleviate the effects of far-field boundary conditions on the simulations, the large computational domain size is set as $[25D, 15D]$ where the location of the cylinder centre is $(7.5D, 7.5D)$ and the final time $t = 300$ as well as the spatial resolutions are applied as $dp = 1/10, 1/20$ and $1/30$ for the convergence study.

Figure 5 shows the velocity contour ranging from 1.8×10^{-3} to 1.5 using Wendland and Laguerre-Gauss kernels under the Reynolds number $Re = 100$ under the resolution $dp = 1/6$ at $t = 300$. It can be seen that the method using Laguerre-Gauss kernel efficiently captures the vortex street while that using Wendland kernel fails to present the same physical phenomenon, indicating that the proposed kernel is more effective in reducing numerical errors and thus obtaining more accurate results.

We further verify the correctness of the proposed kernel with three resolutions by comparing convergent drag and lift coefficients with other experimental and simula-

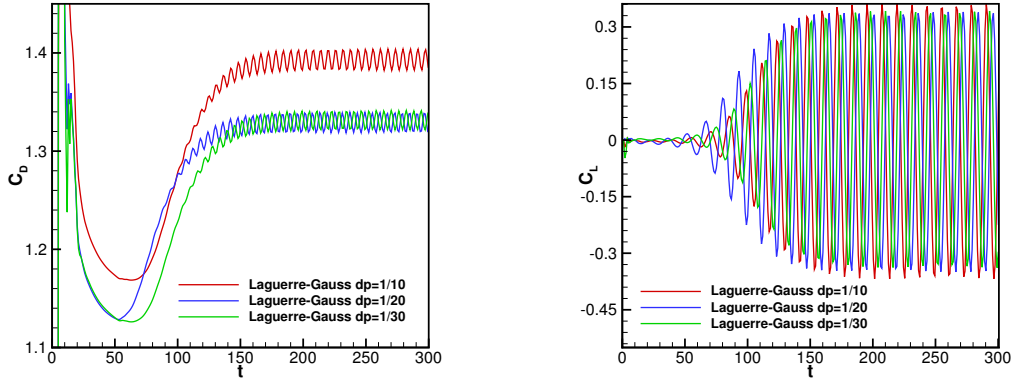


Figure 6: Flow around a cylinder: Drag (left panel) and lift (right panel) coefficients with the time using Laguerre-Gauss kernel with $Re = 100$.

Table 5: Flow around a cylinder: Drag and lift coefficients from different experimental and simulation results at $Re = 100$ and the result using Laguerre-Gauss kernel with the resolution $dp = 1/30$.

Parameters	C_D	C_L	S_t
White[29]	1.46	-	-
Khademinejad et al.[30]	$1.30 \pm -$	± 0.292	0.152
Chiu et al.[31]	1.35 ± 0.012	± 0.303	0.166
Le et al.[32]	1.37 ± 0.009	± 0.323	0.160
Brehm et al.[33]	1.32 ± 0.010	± 0.320	0.165
Liu et al.[34]	1.35 ± 0.012	± 0.339	0.165
Present	1.33 ± 0.009	± 0.340	0.169

tion results listed in Table 5 where the result of using extended Eulerian SPH with Laguerre-Gauss kernel is denoted as "Present". Figure 6 presents the drag and lift coefficients calculated by Eulerian SPH method using Laguerre-Gauss kernel under three resolutions from $dp = 1/10$ to $dp = 1/30$ until the final time $t = 300$, showing that the drag coefficients reach a stable value after a period of fluctuation at the beginning while the lift coefficient oscillates around zero. From Figure 6 and Table 5, it can be obtained that the results of drag and lift have converged and are in agreement with other references, indicating that the results can be considered correct. In the present study, the computations are all performed on an Intel Core i7-10700 2.90 GHz 8-core desktop computer and the CPU wall-clock times obtained by extended Eulerian SPH method using Wendland and Laguerre-Gauss kernels with the spatial resolution $dp = 1/10$ are 4604.81s and 4818.91s in the whole process, respectively, indicating that the computational efficiency of using both kernels is comparable.

4.4. 2D oscillating plate

In 2D solid dynamics, following Refs. [19, 35, 36], the oscillating plate with the length $L = 0.2m$ and the thickness $H = 0.02m$ where one edge is fixed and the other edges are free is studied to verify the accuracy of Laguerre-Gause kernel. In the case, the density $\rho_0 = 1000.0kg/m^3$, Young's modulus $E = 2$ MPa, physical time $t = 2s$ and Poisson's ratio ν is changeable. Also, the initial velocity is perpendicular to the plate strip given by

$$v_y = v_f c \frac{f(x)}{f(L)}, \quad (30)$$

with v_f denoting a constant and $f(x)$ written as

$$f(x) = \frac{(\sin(kL) + \sinh(kL))(\cos(kx) - \cosh(kx)) - (\cos(kL) + \cosh(kL))(\sin(kx) - \sinh(kx))}{(\sin(kL) + \sinh(kL))(\cos(kL) - \cosh(kL)) - (\cos(kL) + \cosh(kL))(\sin(kL) - \sinh(kL))}. \quad (31)$$

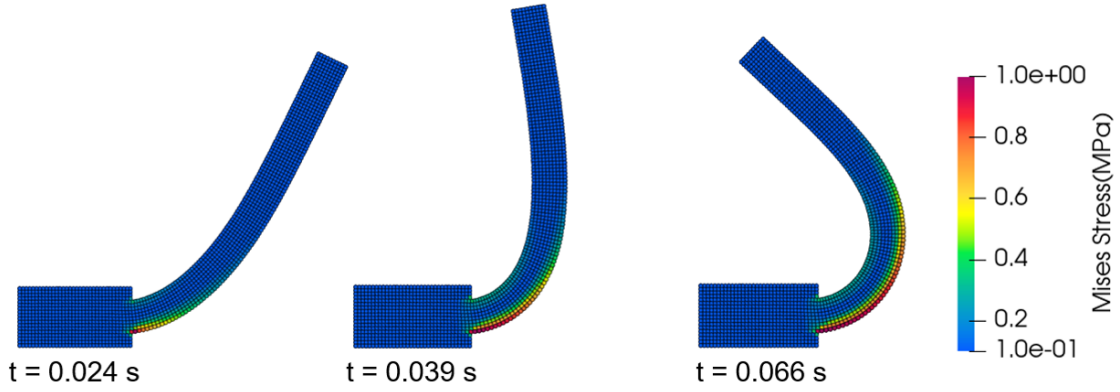


Figure 7: 2D oscillating plate: The Mises stress contour ranging from 0.1 MPa to 1.0 MPa using Laguerre-Gauss kernel with $\nu_f = 0.15$ and Poisson's ratio $\nu = 0.3975$ under the spatial resolution $H/dp = 10$.

Here, k is derived by

$$\cos(kL) \cosh(kL) = -1, \quad (32)$$

with $kL = 1.875$. Also, the theoretical frequency ω is given by

$$\omega^2 = \frac{EH^2k^4}{12\rho(1-\nu^2)}. \quad (33)$$

To keep the results reasonable, the largest spatial resolution is set as $H/dp = 10$ in the case to discretize the computational domain and other two spatial resolutions $H/dp = 20$ and 40 are applied for the convergence study [19, 35, 36].

Figure 7 presents the Mises stress contour ranging from 0.1 MPa to 1.0 MPa using Laguerre-Gauss kernel with the resolution as $H/dp = 10$, proving that the results obtained by the proposed kernel are smooth. Also, Figure 8 shows the vertical position y at the midpoint of the plate strip end using Laguerre-Gauss kernel among the three resolutions and the comparison with that using Wendland kernel with $H/dp = 10$. It can be seen that as the resolution increases, the gap between the different resolutions decreases and therefore the results are convergent and achieve

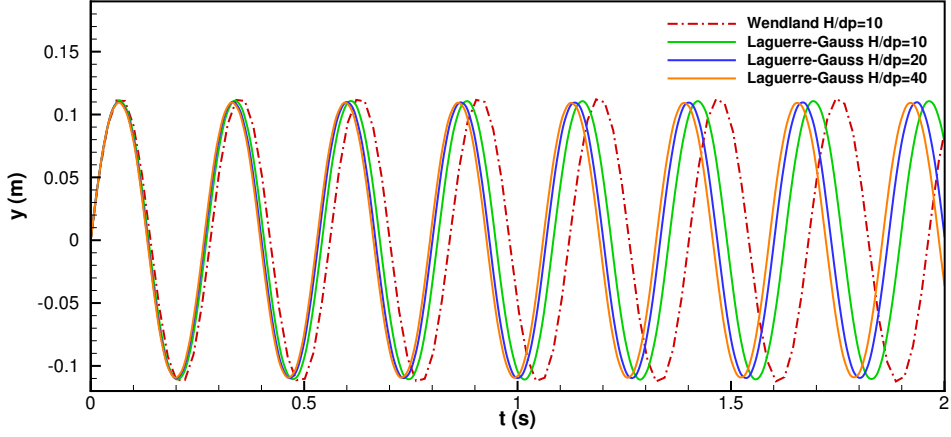


Figure 8: 2D oscillating plate: The vertical position y located at the midpoint of the plate strip end [19] using Laguerre-Gauss kernel with the $v_f = 0.05$ and Poisson's ratio $\nu = 0.3975$ under the spatial resolution as $H/dp = 10, 20$ and 40 , and the comparison with the result using Wendland kernel at $H/dp = 10$. In this case, the theoretical oscillation period $T_{\text{Theoretical}} = 0.254$ and the oscillation periods using truncated Laguerre-Gauss and Wendland kernels are $T_{\text{LG}} = 0.271$ with $\text{Error}_{\text{LG}} = 6.7\%$ and $T_{\text{W}} = 0.282$ with $\text{Error}_{\text{W}} = 11.0\%$, respectively.

Table 6: 2D oscillating plate: The oscillation period using Wendland and Laguerre-Gauss kernels with various v_f and ν under the spatical resolution $H/dp = 10$ and the comparisons with the theoretical results.

v_f	ν	$T_{\text{Theoretical}}$	T_{W}	Error_{W}	T_{LG}	Error_{LG}
0.05	0.22	0.27009	0.29792	10.3%	0.28824	6.7%
0.1	0.22	0.27009	0.29721	10.0%	0.29016	7.4%
0.05	0.3	0.26412	0.291416	10.3%	0.28184	6.7%
0.1	0.3	0.26412	0.29130	10.3%	0.28138	6.5%
0.05	0.4	0.25376	0.28012	10.4%	0.27072	6.9%
0.1	0.4	0.25376	0.28065	10.6%	0.27134	6.5%

second-order convergence. Additionally, Laguerre-Gauss kernel demonstrates the ability to attain a more precise oscillation period than Wendland kernel. However, it is worth noting that the achieved improvement in accuracy is relatively modest when contrasted with previous simulations. This is primarily attributed to the fact that the outcomes obtained by the latter kernel at lower resolutions are already in close proximity to the theoretical oscillation period. For quantitative analysis, two kernels are applied to calculate the oscillation period T separately at low resolution $H/dp = 10$ to verify the performance. Table 6 lists the oscillation period and errors using Wendland (denoted as T_W and $Error_W$, respectively) and Laguerre-Gauss (denoted as T_{LG} and $Error_{LG}$, respectively) kernels with different v_f and ν compared with the theoretical oscillation period (denoted as $T_{Theoretical}$) under the resolution $H/dp = 10$, clearly showing that the errors of using Laguerre-Gauss kernel are much smaller than that of using Wendland kernel. Furthermore, the CPU wall-clock times obtained by total Lagrangian SPH using Wendland and Laguerre-Gauss kernels at the spatial resolution $dp = 1/40$ in whole process are 537.68s and 530.25s, implying that the computational efficiency of using both kernels is comparable.

4.5. 3D oscillating plate

In this section, we simulate the oscillation of a 3D thin plate to validate the robustness and accuracy of the truncated Laguerre-Gauss kernel in 3D dimensions. Following Refs. [37, 38, 39], a square plate is set as the length $L = 0.4m$, width $W = 0.4m$ and height $H = 0.01m$ with the density $\rho_0 = 1000.0kg/m^3$, Young's modulus $E = 100.0$ MPa and Poisson's ratio $\nu = 0.3$ and the simulation time is $t = 0.1s$. Under the condition that the support effect is applied on the centerline of lateral faces, i.e. the corresponding particle is fixed in the z -direction, the initial

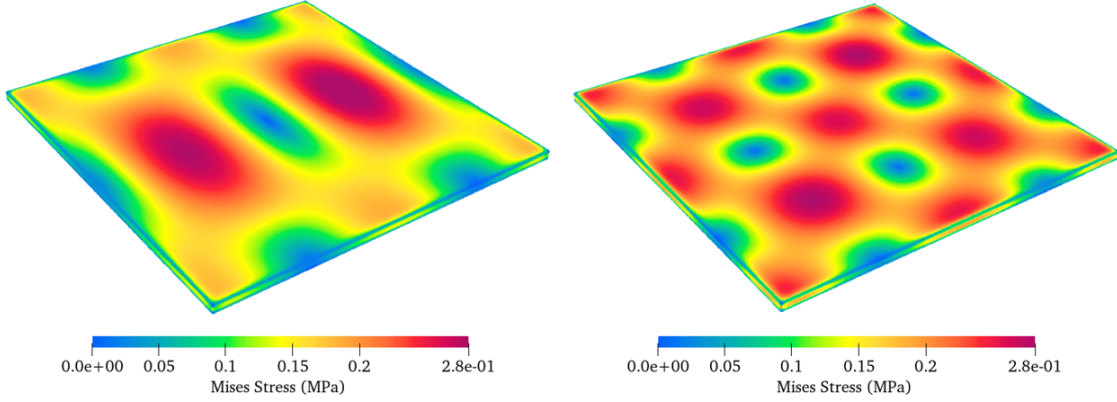


Figure 9: 3D oscillating plate: The Mises stress contour ranging from 0 MPa to 0.28 MPa with the vibration mode of $(m, n) = (2, 1)$ at $t = 0.00279s$ (left panel) and $(m, n) = (2, 2)$ at $t = 0.00219s$ (right panel) using Laguerre-Gauss kernel with the spatial resolution $H/dp = 9$.

velocity v_z along the z -direction is given as

$$v_z(x, y) = \sin \frac{m\pi x}{L} \sin \frac{n\pi y}{W}, \quad (34)$$

where m and n control the x - and y - directional vibration modes, respectively. Also, the theoretical vibration period of the plate is given by

$$T = \frac{2}{\pi} \left[\left(\frac{m}{L} \right)^2 + \left(\frac{n}{W} \right)^2 \right]^{-1} \sqrt{\frac{\rho H}{D}}, \quad (35)$$

with the flexural rigidity $D = EH^3/[12(1 - \nu^2)]$. Also, we apply three spatial resolutions $H/dp = 5, 7$ and 9 in the case.

Figure 9 presents the Mises stress contour ranging from 0 MPa to 0.28 MPa with the vibration mode of $(m, n) = (2, 1)$ at $t = 0.00279s$ and $(m, n) = (2, 2)$ at $t = 0.00219s$ using Laguerre-Gauss kernel with the spatial resolution $H/dp = 9$, showing the proposed kernel enable obtain smooth results of Mises stress. Also, Figure 10 illustrates the oscillation period of the kinetic energy for the vibration mode $(m, n) = (2, 1)$ and $(2, 2)$ using Laguerre-Gauss kernel at three different resolutions

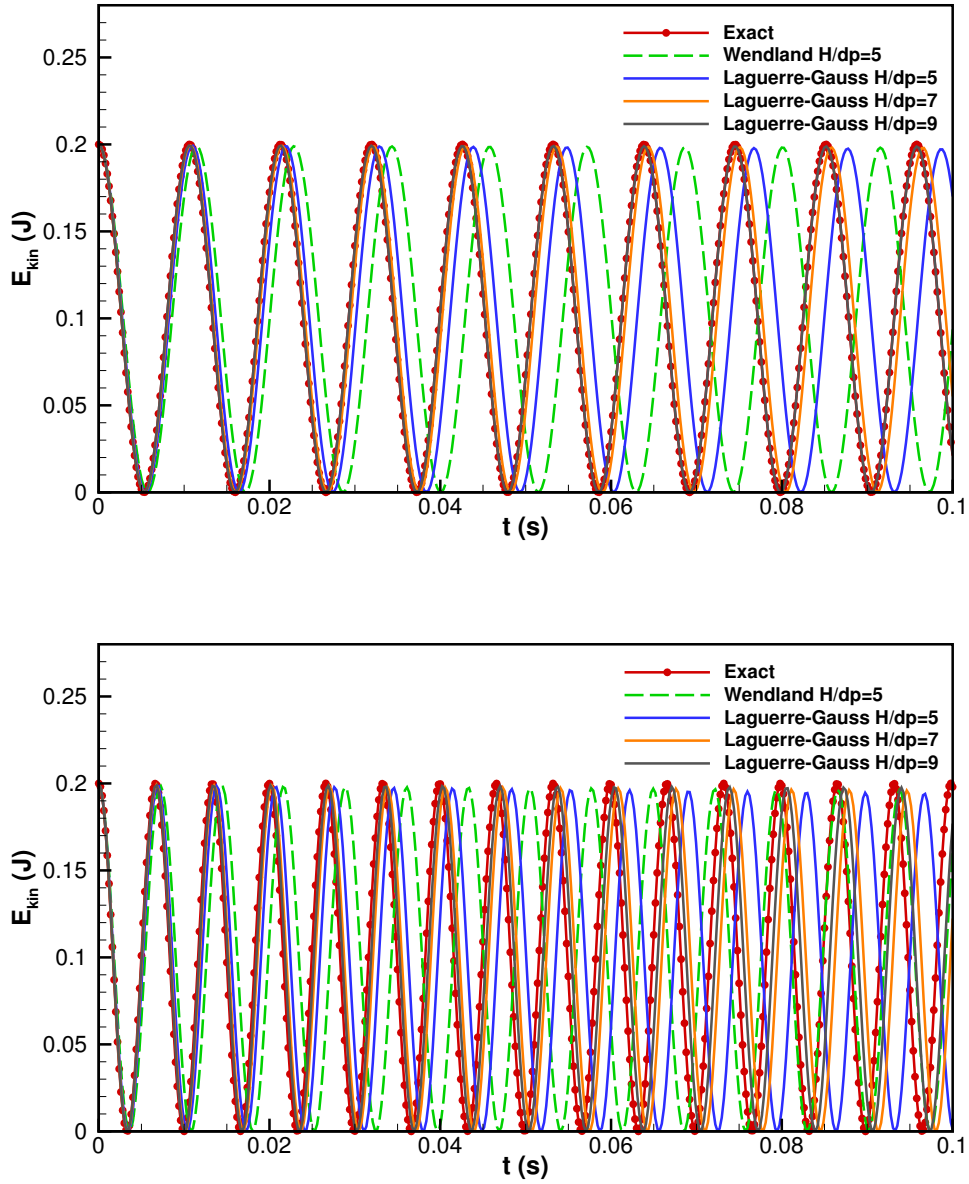


Figure 10: 3D oscillating plate: The oscillation period of the kinetic energy for the vibration mode of $(m, n) = (2, 1)$ (upper panel) and $(2, 2)$ (bottom panel) using Laguerre-Gauss kernel with the spatial resolution as $H/dp = 5, 7$ and 9 , and the comparisons with the results using Wendland kernel with $H/dp = 5$ and the theoretical solutions denoted as "Exact".

$H/dp = 5, 7$ and 9 and the comparison with the results using Wendland kernel with $H/dp = 5$ and the theoretical solution, implying that Laguerre-Gauss kernel is able to obtain higher accuracy. Analogous to the preceding example, the enhancement in accuracy using the proposed kernel is relatively marginal due to the same reason. Besides, it is observed that with the increase of spatial resolutions, the results are convergent. The wall-clock time for simulation of the vibration mode of $(m, n) = (2, 1)$ obtained by total Lagrangian SPH using Wendland and Laguerre-Gauss kernels with spatial resolution $H/dp = 9$ in whole process are approximately $21910.9s$ and $21906.0s$, respectively, showing that the computational efficiency of using Laguerre-Gauss kernel is at the same level as that of using Wendland kernel.

4.6. 3D Bending column

We also consider a bending-dominated problem called bending column to investigate the robustness and accuracy of Laguerre-Gauss kernel further. Following Refs. [40, 19], a rubber-like material with a length of $L = 6m$, a height of $H = 1m$ and a square cross-sectional area which is fixed at the bottom is applied in the numerical simulations, while the initial velocity conditions are given as $\mathbf{v}_0 = 10(\frac{\sqrt{3}}{2}, \frac{1}{2}, 0)^T$, density $\rho_0 = 1100kg/m^3$, Young's modulus $E = 17$ MPa and Poisson's ratio $\nu = 0.45$. Also, three spatial resolutions including $dp = 1/6$, $dp = 1/12$ and $dp = 1/24$ are applied for the convergence study.

Figure 11 presents the Mises stress contour ranging from 0 MPa to 2.8 MPa using Laguerre-Gauss kernel with the spatial resolution $H/dp = 12$, indicating that the results are smooth by using the proposed kernel. Besides, Figure 12 portrays the vertical position z observed at the top of the column [19] using Laguerre-Gauss kernel at three different resolutions $dp = 1/6, 1/12$ and $1/24$, and their comparisons with Wendland kernel at the resolution $dp = 1/6$ as well as the result obtained by Aguirre

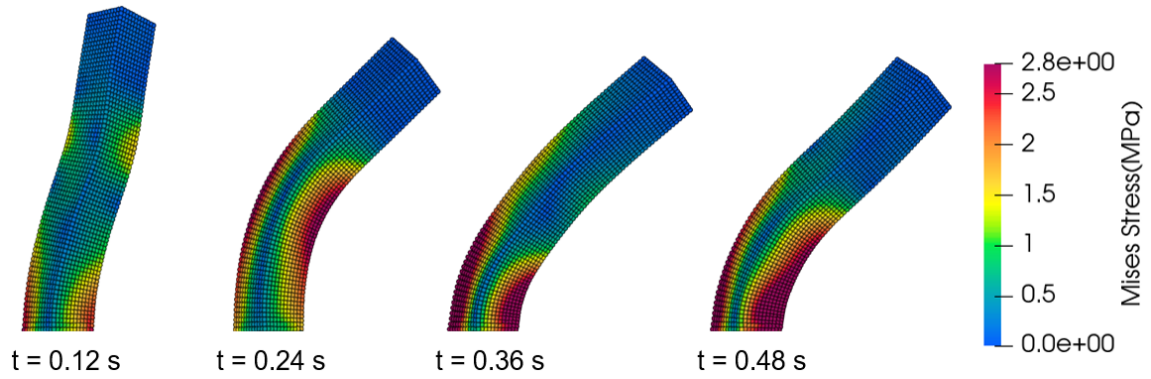


Figure 11: 3D Bending column: The Mises stress contour ranging from 0 MPa to 2.8 MPa using Laguerre-Gauss kernel with the spatial resolution $H/dp = 12$.

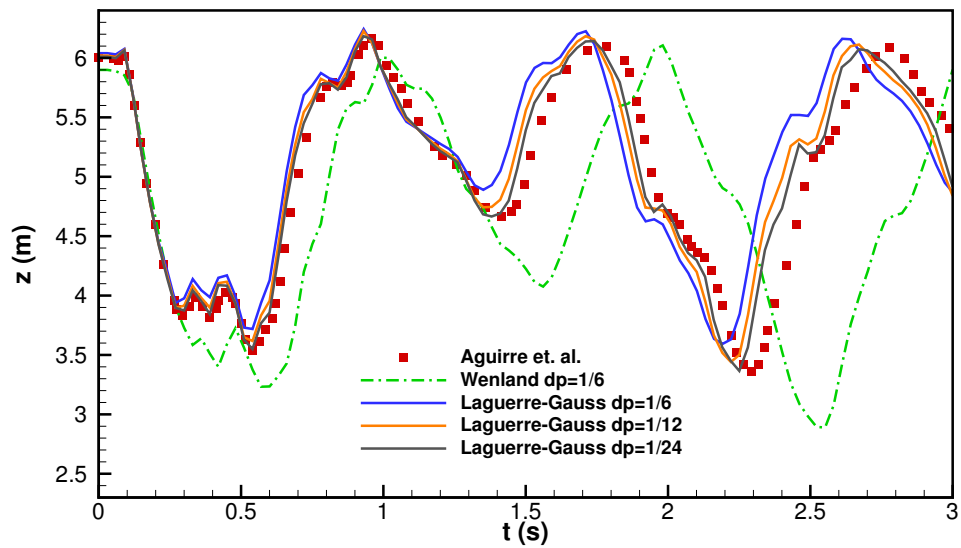


Figure 12: 3D Bending column: The vertical position z located at the top of the column [19] using Wendland and Laguerre-Gauss kernels with three different resolutions and the comparisons with the reference data from Aguirre et al. [41].

et al. [41], showing that Laguerre-Gauss kernel can improve accuracy significantly compared to Wendland kernel as expected and the results converge rapidly with the increase of the spatial resolutions.

5. Summary and conclusion

In this paper, the error of truncated Laguerre-Gauss kernel is analyzed and the results show that the proposed kernel introduces much less truncation error and relaxation residue after particle relaxation than Wendland and Laguerre-Wendland kernels, indicating its considerably improved accuracy and stability. Furthermore, a set of $2D$ and $3D$ numerical examples for fluid dynamics and solid dynamics are tested and have demonstrated that using the proposed kernel enable obtain considerably higher accuracy than Wendland kernel with comparable computational efficiency.

References

- [1] S. Litvinov, X. Hu, N. A. Adams, Towards consistence and convergence of conservative sph approximations, *Journal of Computational Physics* 301 (2015) 394–401.
- [2] L. B. Lucy, A numerical approach to the testing of the fission hypothesis, *The astronomical journal* 82 (1977) 1013–1024.
- [3] J. J. Monaghan, Simulating free surface flows with sph, *Journal of computational physics* 110 (2) (1994) 399–406.
- [4] L. D. Libersky, A. G. Petschek, T. C. Carney, J. R. Hipp, F. A. Allahdadi, High strain lagrangian hydrodynamics: a three-dimensional sph code for dynamic material response, *Journal of computational physics* 109 (1) (1993) 67–75.

- [5] P. Randles, L. D. Libersky, Smoothed particle hydrodynamics: some recent improvements and applications, *Computer methods in applied mechanics and engineering* 139 (1-4) (1996) 375–408.
- [6] S. M. Longshaw, B. D. Rogers, Automotive fuel cell sloshing under temporally and spatially varying high acceleration using gpu-based smoothed particle hydrodynamics (sph), *Advances in Engineering Software* 83 (2015) 31–44.
- [7] H. Gotoh, A. Khayyer, Y. Shimizu, Entirely lagrangian meshfree computational methods for hydroelastic fluid-structure interactions in ocean engineering—reliability, adaptivity and generality, *Applied Ocean Research* 115 (2021) 102822.
- [8] Y. Sun, G. Xi, Z. Sun, A generic smoothed wall boundary in multi-resolution particle method for fluid–structure interaction problem, *Computer Methods in Applied Mechanics and Engineering* 378 (2021) 113726.
- [9] R. A. Gingold, J. J. Monaghan, Smoothed particle hydrodynamics: theory and application to non-spherical stars, *Monthly notices of the royal astronomical society* 181 (3) (1977) 375–389.
- [10] M. Liu, G. Liu, Smoothed particle hydrodynamics (sph): an overview and recent developments, *Archives of computational methods in engineering* 17 (2010) 25–76.
- [11] J. W. Swegle, D. L. Hicks, S. W. Attaway, Smoothed particle hydrodynamics stability analysis, *Journal of computational physics* 116 (1) (1995) 123–134.
- [12] J. P. Morris, *Analysis of smoothed particle hydrodynamics with applications*, Monash University Australia, 1996.

- [13] N. J. Quinlan, M. Basa, M. Lastiwka, Truncation error in mesh-free particle methods, *International Journal for Numerical Methods in Engineering* 66 (13) (2006) 2064–2085.
- [14] H. H. Bui, G. D. Nguyen, Smoothed particle hydrodynamics (sph) and its applications in geomechanics: From solid fracture to granular behaviour and multiphase flows in porous media, *Computers and Geotechnics* 138 (2021) 104315.
- [15] C. Zhang, M. Rezavand, Y. Zhu, Y. Yu, D. Wu, W. Zhang, J. Wang, X. Hu, Sphinxsys: An open-source multi-physics and multi-resolution library based on smoothed particle hydrodynamics, *Computer Physics Communications* 267 (2021) 108066.
- [16] C. Zhang, Y.-j. Zhu, D. Wu, N. A. Adams, X. Hu, Smoothed particle hydrodynamics: Methodology development and recent achievement, *Journal of Hydrodynamics* 34 (5) (2022) 767–805.
- [17] X. Yang, S. Peng, M. Liu, A new kernel function for sph with applications to free surface flows, *Applied Mathematical Modelling* 38 (15-16) (2014) 3822–3833.
- [18] Y. Zhu, C. Zhang, Y. Yu, X. Hu, A cad-compatible body-fitted particle generator for arbitrarily complex geometry and its application to wave-structure interaction, *Journal of Hydrodynamics* 33 (2) (2021) 195–206.
- [19] D. Wu, C. Zhang, X. Tang, X. Hu, An essentially non-hourglass formulation for total lagrangian smoothed particle hydrodynamics, *Computer Methods in Applied Mechanics and Engineering* 407 (2023) 115915.
- [20] J. Vila, On particle weighted methods and smooth particle hydrodynamics, *Mathematical models and methods in applied sciences* 9 (02) (1999) 161–209.

- [21] E. F. Toro, M. Spruce, W. Speares, Restoration of the contact surface in the hll-riemann solver, *Shock waves* 4 (1) (1994) 25–34.
- [22] E. F. Toro, The hllc riemann solver, *Shock waves* 29 (8) (2019) 1065–1082.
- [23] E. F. Toro, *Riemann solvers and numerical methods for fluid dynamics: a practical introduction*, Springer Science & Business Media, 2013.
- [24] Z. Wang, C. Zhang, O. J. Haidn, X. Hu, An eulerian sph method with weno reconstruction for compressible and incompressible flows, *Journal of Hydrodynamics* (2023) 1–12.
- [25] C. Zhang, X. Hu, N. A. Adams, A weakly compressible sph method based on a low-dissipation riemann solver, *Journal of Computational Physics* 335 (2017) 605–620.
- [26] H. Wendland, Piecewise polynomial, positive definite and compactly supported radial functions of minimal degree, *Advances in computational Mathematics* 4 (1995) 389–396.
- [27] Y. Zhu, X. Hu, An l2-norm regularized incremental-stencil weno scheme for compressible flows, *Computers & Fluids* 213 (2020) 104721.
- [28] G. I. Taylor, A. E. Green, Mechanism of the production of small eddies from large ones, *Proceedings of the Royal Society of London. Series A-Mathematical and Physical Sciences* 158 (895) (1937) 499–521.
- [29] F. M. White, J. Majdalani, *Viscous fluid flow*, Vol. 3, McGraw-Hill New York, 2006.

- [30] T. Khademinezhad, P. Talebizadeh, H. Rahimzadeh, Numerical study of unsteady flow around a square cylinder in compare with circular cylinder, in: Conference Paper, 2015.
- [31] P.-H. Chiu, R.-K. Lin, T. W. Sheu, A differentially interpolated direct forcing immersed boundary method for predicting incompressible navier–stokes equations in time-varying complex geometries, *Journal of Computational Physics* 229 (12) (2010) 4476–4500.
- [32] D.-V. Le, B. C. Khoo, J. Peraire, An immersed interface method for viscous incompressible flows involving rigid and flexible boundaries, *Journal of Computational Physics* 220 (1) (2006) 109–138.
- [33] C. Brehm, C. Hader, H. F. Fasel, A locally stabilized immersed boundary method for the compressible navier–stokes equations, *Journal of Computational Physics* 295 (2015) 475–504.
- [34] C. Liu, X. Zheng, C. Sung, Preconditioned multigrid methods for unsteady incompressible flows, *Journal of Computational physics* 139 (1) (1998) 35–57.
- [35] J. P. Gray, J. J. Monaghan, R. Swift, Sph elastic dynamics, *Computer methods in applied mechanics and engineering* 190 (49-50) (2001) 6641–6662.
- [36] L. D. Landau, *Course of theoretical physics, Theory of elasticity* 10 (1986) 32–35.
- [37] A. W. Leissa, *Vibration of plates vol. 160: Scientific and technical information division, National Aeronautics and Space Administration* 43 (1969) 1651–1663.

- [38] A. Khayyer, H. Gotoh, Y. Shimizu, Y. Nishijima, A 3d lagrangian meshfree projection-based solver for hydroelastic fluid-structure interactions, *Journal of Fluids and Structures* 105 (2021) 103342.
- [39] A. Khayyer, Y. Shimizu, H. Gotoh, S. Hattori, A 3d sph-based entirely lagrangian meshfree hydroelastic fsi solver for anisotropic composite structures, *Applied Mathematical Modelling* 112 (2022) 560–613.
- [40] C. Zhang, J. Wang, M. Rezavand, D. Wu, X. Hu, An integrative smoothed particle hydrodynamics method for modeling cardiac function, *Computer Methods in Applied Mechanics and Engineering* 381 (2021) 113847.
- [41] M. Aguirre, A. J. Gil, J. Bonet, A. A. Carreno, A vertex centred finite volume jameson–schmidt–turkel (jst) algorithm for a mixed conservation formulation in solid dynamics, *Journal of Computational Physics* 259 (2014) 672–699.